Analysis of magneto-natural-convection flow in a semi-annulus enclosure filled with a micropolar-nanofluid; A computational framework using CVFEM and FVM

Seyyed Masoud Seyyedi [1,2*], M. Hashemi-Tilehnoee [3], E. Palomo del Barrio [3,4], A.S. Dogonchi [5], M. Sharifpur [6,7,*]

[1] Department of Mechanical Engineering, Aliabad Katoul Branch, Islamic Azad University, Aliabad Katoul, Iran

[2] Energy Research Center, Aliabad Katoul Branch, Islamic Azad University, Aliabad Katoul, Iran

[3] Centre for Cooperative Research on Alternative Energies (CIC energiGUNE), Basque Research and Technology Alliance (BRTA), Alava Technology Park, Albert Einstein 48, 01510 Vitoria-Gasteiz, Spain

[4] IKERBASQUE Basque Foundation for Science, Plaza Euskadi 5, 48009 Bilbao, Spain

[5] Independent researcher in Mechanical Engineering, Iran

[6] Department of Mechanical and Aeronautical Engineering, University of Pretoria, Pretoria 0002, South Africa

[7] Department of Medical Research, China Medical University Hospital, China Medical University, Taichung, Taiwan

[*]corresponding authors: (Seyyed Masoud Seyyedi) s.masoud_seyedi@aliabadiau.ac.ir ,

(M. Sharifpur) mohsen.sharifpur@up.ac.za

Abstract

Micropolar fluids are the media in which their behavior is affected by the microrotation of the substructure particles. In the present work, the natural-convection flow of a micropolar-nanofluid (Al_2O_3/water) in the presence of an inclined magnetic field in a semi-annulus enclosure is investigated. The influence of active parameters on magneto-natural convection is investigated. The governing equations (mass, momentum, microrotation, and energy) are numerically solved by CVFEM. Moreover, for some conservative comparisons, the equations are solved by Ansys Fluent CFD code which is conjugated by an innovative nondimensionlization scheme. The effects of important parameters are investigated on the streamlines, isotherms, microrotation contours, the maximum absolute value of stream function ($|\Psi_{max}|$) , the average Nusselt number (Nu_{ave}) and the maximum absolute value of microrotation ($|N^*_{max}|$). The results discovered that the values of Nu_{ave} descend with ascending the Hartmann number (Ha) and material parameter (K) while it ascends with ascending Rayleigh number (Ra) and particle volume fraction (ϕ). The value of Nu_{ave} descends 10.8% while $|N^*_{max}|$ increases 19.8% when K increases from 1 to 2. The value of Nu_{ave} descends 44.83% when Ha increases from 25 to 75 at $\lambda = 45°$. The minimum value of Nu_{ave} occurs at $\lambda = 45°$ for $Ha = 25$ and at $\lambda = 30°$ for $Ha = 50$ and $Ha = 75$.

Keywords: Microplor, Nanofluid, Heat transfer, Inclined magnetic field, CVFEM, FVM

1. Introduction

In recent years low thermal conductivity (TC) of fluids used in thermal-related devices which can result in poor performance of them, is the main challenge among researchers. To tackle this issue, some solutions have been proposed in order to boost the fluids TC the very epitome of which may be adding nano-scaled materials to the base liquid. This combination which is called nanofluids (NFs) and has TC higher than normal liquids was initially recognized by Choi [1]. At the identical time, the investigation of natural convection (NC) considering such a mixture attracts much attention from researchers owing to its wide application in many practical and industrial areas, for instance, solar collectors, electronic devices, and geothermal operations. The impact of the thermic sink position and size on the NC within a sloping porous enclosure considering Cu-H_2O NF inside was examined by Rashad et al. [2]. Heat transfer (HT) augmentation within annuli utilizing diverse types of NFs studied by Abu-Nada et al. [3]. They found for high value of Ra, nanoparticles with higher TC could lead to increased heat transfer. Numerical analysis of NC and entropy in a C-like chamber loaded with CuO-H_2O NF and impacted by a constant magnetic field was performed by Chamkha et al. [4]. The Brownian motion impact was also considered in this work. They concluded that the nanoparticle volume fraction improves natural convection while undesirably increasing the rate of entropy generation. They also revealed that the magnetic field may lessen both of them. Sheikhzadeh et al. [5] perused the heat transmission features of NF within a container with partly active walls during the NC process. They apperceived Ra and volume fraction of nano-materials have a positive influence on the rate of heat transfer. The impacts of heat generation and various types of barriers on the magnetized NC and entropy of NF-loaded container were examined by Selimefendigil and Oztop [6]. The outcomes indicated that obstacles utilized in this study could worsen the HT process mostly for higher Ra while the existence of nano-materials boosts the rate of HT. Alsabery et al. [7] examined HT of NC within a porous domain having a wavy surface and loaded with NF. This study was performed considering the local thermic-non-equilibrium situation and in which the heater position and its length on NC were also analyzed. They reported the length and location of the heater and concentration of nano-materials may play a major role in managing HT within the domain. Thermosolutal convection analysis inside a domain with NF and some fins inside impacted by magnetic field and Soret and Dufour parameters was done by Aly et al. [8]. They reported buoyancy parameter has the main role in administrating the strength and orientation of particles' dispersions inside the domain. Gholamalipour et al. [9] analyzed the eccentricity impacts of a hot source in an NF-filled porous domain on the entropy and NC features. They proved for varying eccentricity HT may be boosted or worsened and it is strongly dependent on the amount of Ra and orientation of interior cylinder motion. Tayebi and Chamkha [10] performed a numerical investigation on the entropy and NC of magnetized hybrid NF in a domain considering a conducting cylinder inside and Brownian motion. The findings indicated that an empty conducting cylinder would play a momentous role in managing HT rate and irreversibilities inside the domain. Gorla et al. [11] simulated NC in an NF-filled porous domain affected by a heat sink/source. They detected the heat source position and volume fraction of nano-

materials could affect the rate of HT considerably. Seyyedi et al. [12-13] investigated natural convection and entropy generation analyses inside the cavities filled with nanoparticles encapsulated phase change material by applying the impact of the inclined magnetic field. Abdel-Nour et al. [14] perused entropy and magnetic NC in a porous domain heated from left and bottom-sided and filled with NF. The outcomes showed both entropy and HT rate grows with rising Ra while they lessened when one boosts the strength of the magnetic field. Seyyedi et al. [15] investigated changes in entropy generation for different shapes of nanoparticles. They found that the entropy generation number ascends by ascending the nanoparticle percent. In a porous chamber filled with nanofluid, Hashemi-Tilehnoee et al. [16] performed the second law analysis. The entropy generation number and average Nusselt number were calculated for magneto-hydrodynamic (MHD) flow inside a semi-annulus enclosure by Seyyedi et al. [17-18]. Researchers are now focusing on a novel kind of liquids called Micro-polar-fluids (MPFs) in which the intrinsic motions of molecules of liquids and their micro-structure may be taken into account. Micropolar fluids are fluids with microstructure. They belong to a class of fluids with nonsymmetric stress tensor that we shall call polar fluids, and include, as a special case, the well-established Navier-Stokes model of classical fluids that we shall call ordinary fluids. Physically, micropolar fluids may represent fluids consisting of rigid, randomly oriented (or spherical) particles suspended in a viscous medium, where the deformation of fluid particles is ignored. Eringen [19-20] was the first researcher who proposes this type of liquid. Micropolar fluids take into account the microstructure of the fluid along with the inertial characteristics of the substructure particles, which are allowed to undergo rotation. Such fluids have many engineering applications i.e. exotic lubricants, animal blood, and polymer streams. In such a way micropolar nanofluid (MPNF) can be considered as a fluid medium whose properties and behavior are strongly influenced by the local motions of the material particles contained in each of its volume elements. Investigation of such fluids without/with nano-materials during NC processes fascinates many researchers. Aydin and Pop [21] analyzed the NC inside a tetrahedral domain heated partly from the left side and filled with a MPF. It was reported MPF presents a lower HT rate in comparison to Newtonian liquids. In other work, in a differentially heated square container filled with a micropolar fluid, they investigated natural convection [22]. Saleem et al. [23] studied th NC flow of MPF within a rectangle-shaped domain warmed from the bottom side. They expressed that ascending the figures of vortex viscosity parameter (K) could lessen the rate of HT. The conjugate NC inside a micropolar nanofluid occupied domain considering local thermal non-equilibrium theory was perused by Mehryan et al. [24]. It was demonstrated the strength of micro-rotations can be boosted by growing K. A numerical examination of the HT features of MPNF in a domain partly sinusoidally warmed during the NC process was done by Ahmed and Rashad [25]. Yan et al. [26] examined the influence of Ha on the radiative NC within a porous domain having to oblique an oval heater inside and occupied with MPNF. They reported changing the orientation of the heater would play a leading role in controlling HT inside the container. NC flow inside a porous domain influenced by the magnetic field and occupied by MPNF was modeled by Karagiannakis et al. [27].

They concluded the intensity of the magnetic field could manage the HT and flow within the chamber. Izadi et al. [28] explored magnetized HT of MPNF during NC affected by thermal radiation within a porous domain with an elliptic heater inside. Good papers about micropolar nanofluid flow on a stretching sheet have been published by Hsiao [29-32]. He investigated the effects of electrical magneto hydrodynamic (EMHD), radiative and viscous dissipation on the fluid flow.

As it can be seen from the literature review, there are a few works on the MPNFs. Therefore, the goal of the present work is to investigate the active parameters on natural-convection flow of a micropolar-nanofluid (Al_2O_3/water) in a semi-annulus enclosure where the flow is affected by an inclined magnetic field.

The importance of this research compared to previous studies can be summarized as follows:

1. The working fluid is considered to be a micropolar nanofluid (Al_2O_3/water).
2. An inclined magnetic field affects fluid flow.
3. The effects of main parameters such as $\mathrm{Ra}, \mathrm{Ha}, \lambda, , A, N_u, \phi$ and K are investigated on heat transfer.
4. The microrotation equation is simultaneously solved with momentum equations.

In summary, the innovation of the present work is the simultaneous investigation of the natural heat transfer of a micropolar nanofluid in a complex geometry considering the magnetic field.

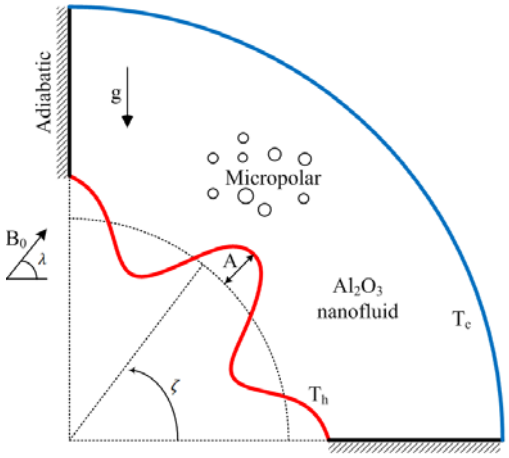

Fig. 1: Schematic view of the considered problem

2. Problem definition

The schematic diagram of the problem is shown in Fig. 1. The temperatures of the inner and outer walls are T_h and T_c, respectively whereas the two other walls are thermally insulated. The fluid flow is affected by an external uniform magnetic field ($B_0 = \left(B_x^2 + B_y^2\right)^{1/2}$ and $\lambda = \tan^{-1}\left(B_y/B_x\right)$). The profile of the inner wall follows the pattern [18]:

$$r = r_{in} + A\cos(N_u(\zeta - \zeta_0)) \quad (1)$$

Where N_u and A are the number of undulations and amplitude, respectively, and ζ is the rotation angle.

3. Mathematical Model

3.1. Dimensional form of governing equations

Microrotation is added to the basic governing equations as follows: [18, 22]

$$\frac{\partial u}{\partial x} + \frac{\partial v}{\partial y} = 0 \quad (2)$$

$$\rho_{nf}\left(u\frac{\partial u}{\partial x} + v\frac{\partial u}{\partial y}\right) = -\frac{\partial P}{\partial x} + (\mu_{nf} + k)\left(\frac{\partial^2 u}{\partial x^2} + \frac{\partial^2 v}{\partial y^2}\right) + k\frac{\partial N}{\partial y} + \sigma_{nf}B_0^2(v\sin\lambda\cos\lambda - u\sin^2\lambda) \quad (3)$$

$$\rho_{nf}\left(u\frac{\partial v}{\partial x} + v\frac{\partial v}{\partial y}\right) = -\frac{\partial P}{\partial y} + (\mu_{nf} + k)\left(\frac{\partial^2 v}{\partial x^2} + \frac{\partial^2 v}{\partial y^2}\right) - k\frac{\partial N}{\partial x} + \sigma_{nf}B_0^2(u\sin\lambda\cos\lambda - v\cos^2\lambda) + \rho_{nf}g\beta_{nf}(T - T_0) \quad (4)$$

$$\rho_{nf}j\left(u\frac{\partial N}{\partial x} + v\frac{\partial N}{\partial y}\right) = \gamma_{nf}\left(\frac{\partial^2 N}{\partial x^2} + \frac{\partial^2 N}{\partial y^2}\right) - 2\kappa N + \kappa\left(\frac{\partial v}{\partial x} - \frac{\partial u}{\partial y}\right) \quad (5)$$

$$u\frac{\partial T}{\partial x} + v\frac{\partial T}{\partial y} = \alpha_{nf}\left(\frac{\partial^2 T}{\partial x^2} + \frac{\partial^2 T}{\partial y^2}\right) \quad (6)$$

where the effective density (ρ_{nf}) and heat capacitance $(\rho C_p)_{nf}$ of the nanofluid are defined as:

$$\rho_{nf} = \rho_f(1 - \phi) + \rho_s\phi \quad (7)$$

$$(\rho C_p)_{nf} = (\rho C_p)_f(1 - \phi) + (\rho C_p)_s\phi \quad (8)$$

$$\alpha_{nf} = \frac{k_{nf}}{(\rho C_p)_{nf}} \quad (9)$$

$$(\rho\beta)_{nf} = (\rho\beta)_f(1 - \phi) + (\rho\beta)_s\phi \quad (10)$$

Brinkman model [15] predicts the dynamic viscosity of the nanofluid as follows:

$$\mu_{nf} = \frac{\mu_f}{(1 - \phi)^{2.5}} \quad (11)$$

The effective thermal conductivity and electrical conductivity for nanofluid can be calculated by Eqs. (12) and (13), respectively, [33]:

$$\frac{k_{nf}}{k_f} = \frac{k_s + (m - 1)k_f - (m - 1)\phi(k_f - k_s)}{k_s + (m - 1)k_f + \phi(k_f - k_s)} \quad (12)$$

$$\frac{\sigma_{nf}}{\sigma_f} = 1 + \frac{3(\frac{\sigma_s}{\sigma_f} - 1)\phi}{\left(\frac{\sigma_s}{\sigma_f} + 2\right) - (\frac{\sigma_s}{\sigma_f} - 1)\phi} \quad (13)$$

Also, γ_{nf} can be written as [21,22]

$$\gamma_{nf} = \left(\mu_f + \frac{\kappa}{2}\right) j \tag{14}$$

The vorticity (ω) and stream function (ψ) are defined as follows:

$$u = \frac{\partial \psi}{\partial y}, v = -\frac{\partial \psi}{\partial x} \text{ and } \omega = \frac{\partial v}{\partial x} - \frac{\partial u}{\partial y} \tag{15}$$

3.2. Dimensionless form of governing equations

The non-dimensionless variables used here are:

$$\mathrm{X} = \frac{x}{L}, \quad \mathrm{Y} = \frac{y}{L}, \quad \theta = \frac{T - T_c}{T_h - T_c}, \quad \Omega = \frac{\omega L^2}{\nu_f}, \quad N^* = \frac{NL^2}{\nu_f}, \quad \Psi = \frac{\psi}{\nu_f}, \quad j = L^2 \tag{16}$$

where in Eq. (16) $L = r_{out} - r_{in}$. Using the dimensionless parameters, the governing equations can be rewritten as follows:

$$\left[\frac{\partial \Psi}{\partial \mathrm{Y}}\frac{\partial \Omega}{\partial \mathrm{X}} - \frac{\partial \Psi}{\partial \mathrm{X}}\frac{\partial \Omega}{\partial \mathrm{Y}}\right] = \frac{\left(\frac{\mu_{nf}}{\mu_f} + K\right)}{\rho_{nf}/\rho_f}\left(\frac{\partial^2 \Omega}{\partial \mathrm{X}^2} + \frac{\partial^2 \Omega}{\partial \mathrm{Y}^2}\right) - \frac{K}{\rho_{nf}/\rho_f}\left(\frac{\partial^2 N^*}{\partial \mathrm{X}^2} + \frac{\partial^2 N^*}{\partial \mathrm{Y}^2}\right) + \frac{\beta_{nf}}{\beta_f}\frac{\mathrm{Ra}}{\mathrm{Pr}}\frac{\partial \theta}{\partial \mathrm{X}} + \frac{\sigma_{nf}/\sigma_f}{\rho_{nf}/\rho_f}\mathrm{Ha}^2\left(\cos^2\lambda\frac{\partial^2 \Psi}{\partial \mathrm{X}^2} + \sin^2\lambda\frac{\partial^2 \Psi}{\partial \mathrm{Y}^2} + 2\sin\lambda\cos\lambda\frac{\partial^2 \Psi}{\partial \mathrm{X}\,\partial \mathrm{Y}}\right) \tag{17}$$

$$\left[\frac{\partial \Psi}{\partial \mathrm{Y}}\frac{\partial N^*}{\partial \mathrm{X}} - \frac{\partial \Psi}{\partial \mathrm{X}}\frac{\partial N^*}{\partial \mathrm{Y}}\right] = \frac{\left(\frac{\mu_{nf}}{\mu_f} + \frac{K}{2}\right)}{\rho_{nf}/\rho_f}\left(\frac{\partial^2 N^*}{\partial \mathrm{X}^2} + \frac{\partial^2 N^*}{\partial \mathrm{Y}^2}\right) - \frac{2K}{\rho_{nf}/\rho_f}N^* + \frac{K}{\rho_{nf}/\rho_f}\Omega \tag{18}$$

$$\left[\frac{\partial \Psi}{\partial \mathrm{Y}}\frac{\partial \theta}{\partial \mathrm{X}} - \frac{\partial \Psi}{\partial \mathrm{X}}\frac{\partial \theta}{\partial \mathrm{Y}}\right] = \frac{k_{nf}/k_f}{(\rho C_p)_{nf}/(\rho C_p)_f}\frac{1}{\mathrm{Pr}}\left(\frac{\partial^2 \theta}{\partial \mathrm{X}^2} + \frac{\partial^2 \theta}{\partial \mathrm{Y}^2}\right) \tag{19}$$

In non-dimensional form, the vorticity is:

$$\frac{\partial^2 \Psi}{\partial \mathrm{X}^2} + \frac{\partial^2 \Psi}{\partial \mathrm{Y}^2} = -\Omega \tag{20}$$

In Eq. (17), Pr , Ra , Ha and K are the Prandtl number, the Rayleigh number, the Hartmann number, and the material parameter that are defined as follows:

$$\mathrm{Pr} = \frac{\nu_f}{\alpha_f}, \quad \mathrm{Ra} = \frac{g\beta_f L^3 (T_h - T_c)}{\nu_f \alpha_f}, \quad \mathrm{Ha} = B_0 L\sqrt{\frac{\sigma_f}{\mu_f}}, \quad K = \kappa/\mu_f \tag{21}$$

For solving the Eqs. (17) – (19), it must be used from Eqs. (7) – (14).

The boundary conditions as shown in Fig. 1 are:

$$\theta = 1.0 \text{ on the inner curved wall} \tag{22}$$

$\theta = 0.0$ on the outer curved wall

$\frac{\partial \theta}{\partial n} = 0$ on insulation walls

$\Psi = 0$ and $N^* = 0$ on solid boundaries

It should be mentioned that Eqs. (17), (19) and (20) are converted to the classical problems of natural convection for a Newtonian fluid when $\mathrm{K} = 0$ [34].

The local and average Nusselt numbers on the hot circular wall can be expressed as:

$$\mathrm{Nu}_{local} = -\left(\frac{k_{nf}}{k_f}\right)\frac{\partial \theta}{\partial r} \tag{23}$$

$$\mathrm{Nu}_{\mathrm{ave}} = \frac{1}{\pi/2}\int_0^{\pi/2} \mathrm{Nu}_{local}(\zeta)\, d\zeta \tag{24}$$

4. Numerical procedure

4.1. CVFEM by programing

The CVFEM, control volume finite element method, was initially proposed by Saabas and Baliga [35]. This approach combines the fascinating qualities of both the FVM and the FEM. The governing equations were solved using a FORTRAN program based on the CVFEM in this work.

It should be noted that although the physical problem is a semicircular enclosure, it can be transferred to Cartesian coordinates, and then the governing equations can be written in Cartesian coordinates. There are many papers in this field (See. Refs. [12-15,18 and 29]).

4.2. Grid examination

Table 1 shows the findings of the grid independence investigation. $\mathrm{Ra} = 10^5$, $\mathrm{Pr} = 6.2$, $\phi = 0.05$, $\mathrm{Ha} = 50$, $\lambda = 30°$,$K = 2$, $\mathrm{A} = 0.1$, $N_u = 8$ were used in the computations. As a result, 81×241 can be used as the grid size. Table 2 represents the thermo-physical characteristics of water and Al_2O_3 nanoparticles. Also, the shape factor values (m in Eq. 12) can be found in Ref. [33].

Table 1: The effect of grid size on the average Nusselt number

Mesh	51×151	61×181	71×201	81×241	91×271
$\mathrm{Nu}_{\mathrm{ave}}$	2.3216	2.3074	2.2938	2.2856	2.2818

Table 2: Thermo-physical properties of water and alumina [33]

	$\rho(\mathrm{kg/m^3})$	$C_p(\mathrm{J/kgK})$	$k(\mathrm{W/mK})$	$\beta_T\ (1/\mathrm{K})$	$\sigma(S/\mathrm{m})$
Alumina (Al_2O_3)	3970	765	40	0.85×10^{-5}	1×10^{-10}
Pure water	997.1	4179	0.613	21×10^{-5}	0.05

4.3. Validation

Three case-studies for validations are performed in order to validate the results. Firstly, the isotherms and streamlines contours for a square cavity are compared with Aydin and Pop [22], for two different values of the material parameter ($K = 0$ and $K = 2$) when fluid is air ($\mathrm{Pr} = 0.71$) at $\mathrm{Ra} = 10^3$ and $\mathrm{Ra} = 10^5$. This comparison is presented in Fig. 2. Table 3 shows a comparison between the results of the present study and those of previous works. In Table 4, the values of the $\mathrm{Nu}_{\mathrm{ave}}$ are compared for present work and Ref. [22] at different values of the Rayleigh number and the material parameter. Finally, to ensure that the code is valid when the magnetic force is added to the code, another validation is performed that the results are presented in Table 5. For all validations, the results are acceptable.

Table 3: Comparison of averaged Nusselt number in dependence of Rayleigh number

Ra	Zadravec et al. [36]	Davies [34]	Aydin and Pop [22]	Present study
10^3	1.118	1.118	1.118	1.118
10^4	2.263	2.243	2.234	2.246
10^5	4.540	4.519	4.486	4.553
10^6	8.742	8.8	8.945	8.761

Table 4: The effect of K on the average Nusselt number Nuav for different values of Ra when $\mathrm{Pr} = 0.71$

	Ra							
	10^3		10^4		10^5		10^6	
K	Aydin and Pop [22]	Present study	Aydin and Pop [22]	Present study	Aydin and Pop [22]	Present study	Aydin and Pop [22]	Present study
0	1.118	1.118	2.234	2.246	4.486	4.553	8.945	8.761
0.5	1.057	1.0599	1,947	1.9832	4.033	4.1398	7.984	8.2268
1	1.034	1.036	1.771	1.8031	3.729	3.8351	7.433	7.7719
2	1.016	1.017	1.545	1.5706	3.314	3.4091	6.673	7.0618

Table 5: The values of $\mathrm{Nu}_{\mathrm{ave}}$ for different Hartmann number at $\mathrm{Ra} = 10^4$ and $\mathrm{Ra} = 10^5$ when $\mathrm{Pr} = 0.733$

Ra	Ha	Pirmohammadi et al. [37]	Present study	Error (%)
10^4	0	2.29	2.249	1.79
	10	1.97	1.934	1.83
	50	1.06	1.040	1.89
	100	1.02	1.004	1.57
10^5	0	4.62	4.571	1.06
	25	3.51	3.470	1.14
	100	1.37	1.346	1.75

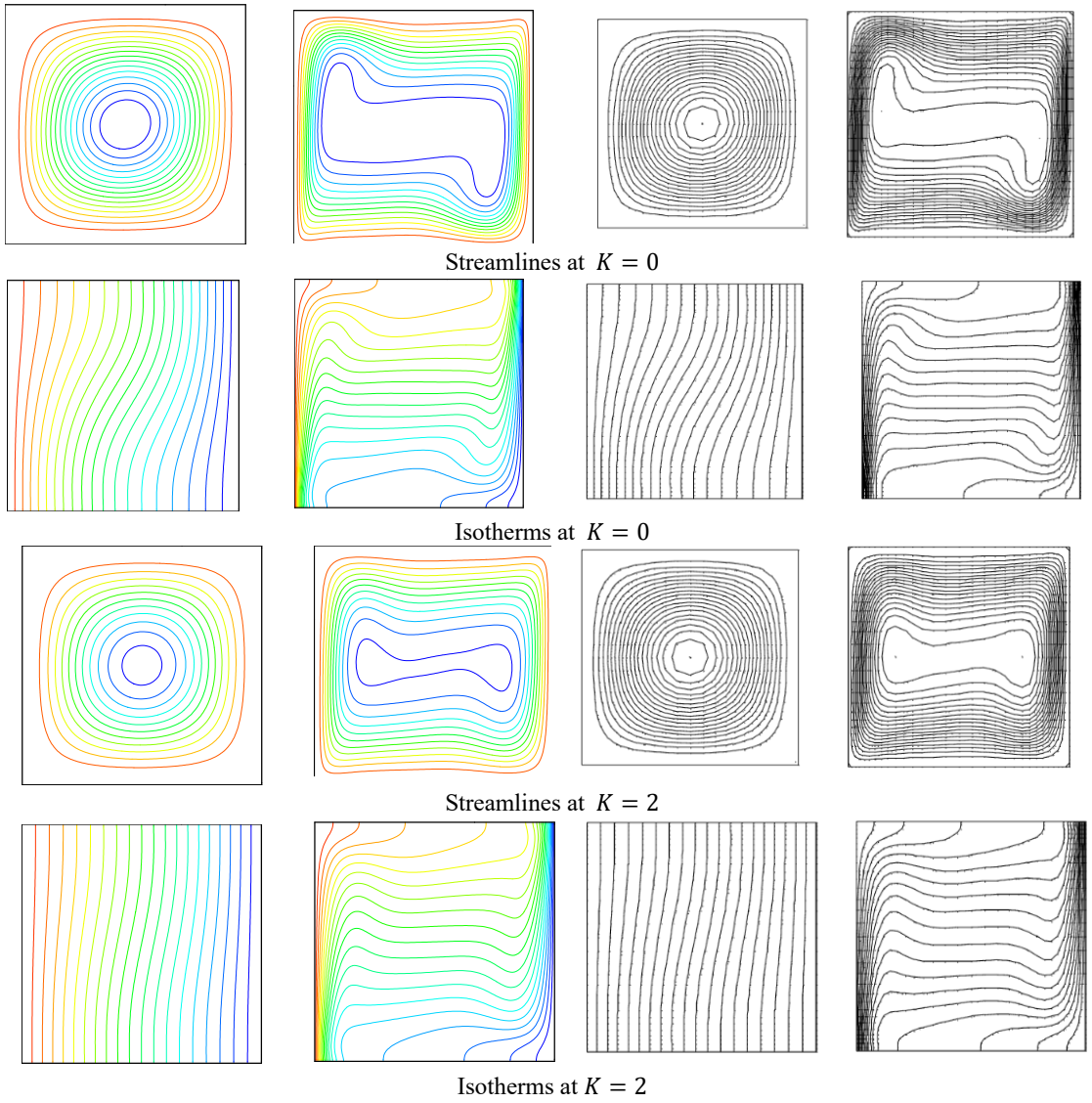

Fig. 2: Comparison for streamlines and isotherms between present work (colored contours) and Aydin and Pop [22] (black & white contours) for $K = 0$ and $K = 2$ at $\mathrm{Ra} = 10^3$ (The first column) and $\mathrm{Ra} = 10^6$ (The second column) when $\mathrm{Pr} = 0.71$

4.4. FVM by Ansys Fluent

Besides the CVFEM code, as a computational framework, the ANSYS Fluent code conjugated by an innovative nondimensionlization scheme, is used to simulate magnetohydrodynamic natural convection in the micropolar nanofluid understudy geometry. The grid verification and validation tests were carried out to ensure the accuracy of the data. The angular momentum of the microrotation effect is introduced by the angular momentum equation to basic equations of Ansys Fluent, as a user-defined scalar (UDS). The boundary conditions also considered the effects of microrotation by the value of the specified flux. The magnetic field is considered in simple form as a source term for momentum equation where joule

heating and viscous effects are neglected in conservation equations of this study. The governing equations are solved using the pressure-based finite volume approach. Except for the buoyancy factor used by the Boussinesq approximation [38], the fluctuation of fluid characteristics with temperature has been disregarded. The edges of the wall are assumed to be smooth and without roughness. For the pressure-velocity coupling [39,40] and formulation of the convection contribution to the coefficients in the finite-volume equations [41,42], the pressure implicit with the splitting of operator (PISO) approach is used [43] . For conservation equations, the convergence criteria are set to 10^{-6}.

5. Results and discussion

In this paper, the free convection heat transfer is numerically studied in a semi-annulus enclosure filled with a micropolar nanofluid. The effects of non-dimensional parameters on the fluid flow are studied. Furthermore, some decision variables are employed for modeling the problem such as Ra , Ha, λ , ϕ, K , A, and N_u. Fig. 3 demonstrates the isotherms, the streamlines, and microrotation contours at Ra $= 10^3, 10^4$ and 10^5. The highest value of the absolute stream function, $|\Psi_{\max}|$, indicates that the power of flow increases as the Ra increases. The values of $|\Psi_{\max}|$ are 0.076, 0.687 and 3.067 for Ra $= 10^3, 10^4$ and 10^5, respectively. When the Ra rises, the center of the inner vortex ascends and is near to the cavity left wall. The form of the isotherms shows how the major heat transfer mechanism varies as the Ra increases. For Ra $= 10^3$, conduction is the predominant heat transfer mechanism compared to convection. The buoyancy forces increase and overcome the viscous forces when the Rayleigh number ascends. Therefore, convection mode overcomes to conduction mode. Also, the isotherms are more distorted at higher Ra since convection effects are stronger. The $\mathrm{Nu}_{\mathrm{ave}}$ increases with ascending the Ra where the values of $\mathrm{Nu}_{\mathrm{ave}}$ are 1.2685, 1.7593 and 4.0405 for Ra $= 10^3, 10^4$ and 10^5, respectively. The increases of $\mathrm{Nu}_{\mathrm{ave}}$ is due to decreasing of thermal boundary layer thickness. The last row in this figure shows the microrotation microplar (N^*) contours for each Rayleigh number. The behavior of N contours are similar to streamlines. The values of $|N^*_{\max}|$ are 0.0636, 0.5703 and 2.4873 for Ra $= 10^3, 10^4$ and 10^5, respectively. These values indicate that there is a stronger rotation for high values of Ra. Other active parameters for this figure are Ha $= 10$, $\lambda = 0°$, $\phi = 0.04$, K $= 2$, $A = 0.1$ and $N_u = 8$.

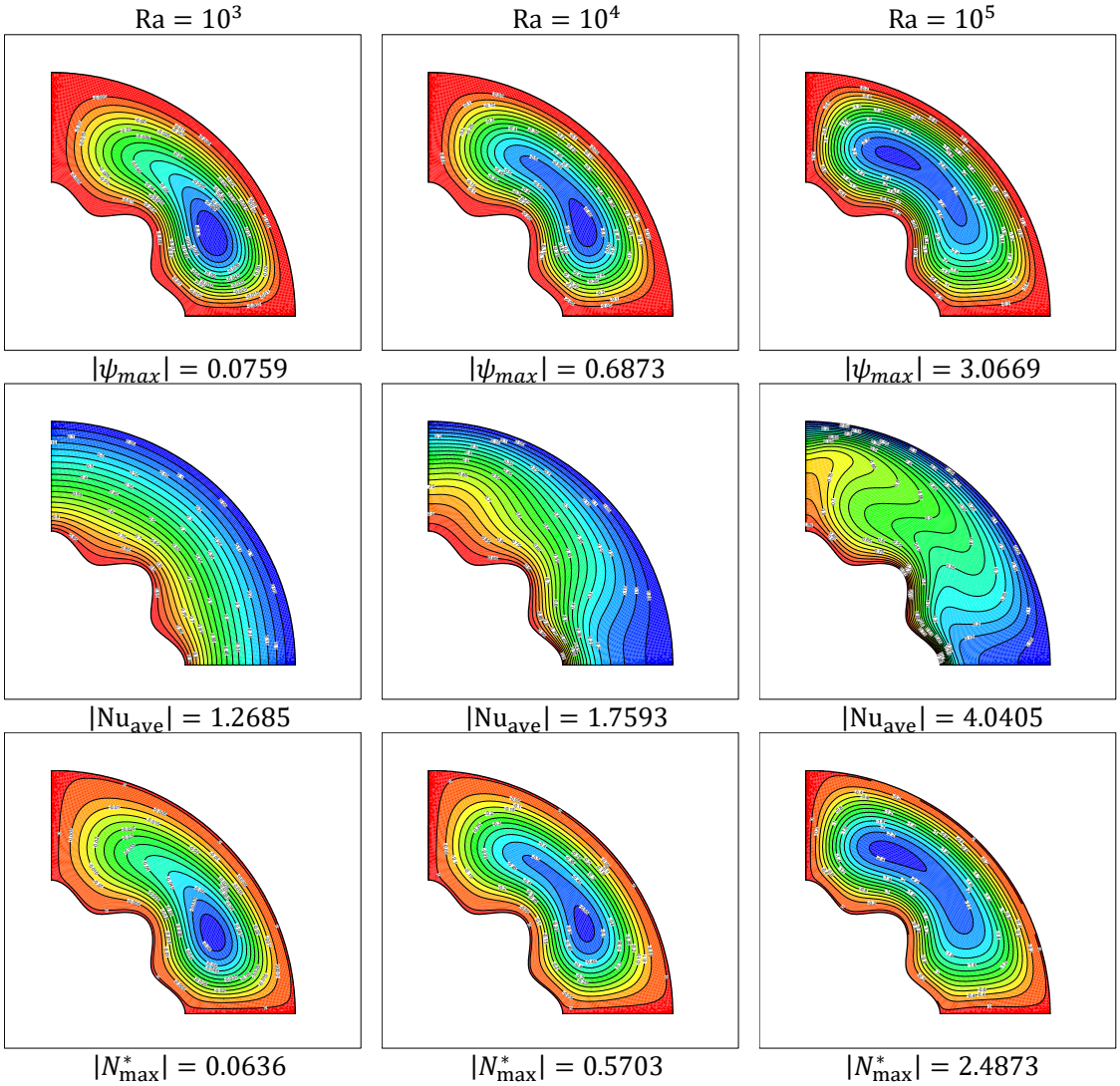

Fig. 3: Streamlines, isotherms, and microrotation contours for three values of Rayleigh number

Fig. 4 reveals the effects of the magnetic field on the isotherms, the streamlines, and microrotation contours for Ha = 0 and Ha = 50 at Ra = 10^5. It is obvious that the flow is suppressed when the Ha increases from 0 to 50 (according to equation 21, the strength of the magnetic field increases with the increase of the Hartmann number). The value of $|\Psi_{max}|$ decreases from 3.325 (without magnetic field) to 1.350 (for Ha = 50). Isotherms show that with increasing Ha, the share of conductive heat transfer mode increases versus convective heat transfer mode. Therefore, the Nu_{ave} decreases from 4.2291 to 2.6207 (38.03% decreasing) with ascending the Ha from 0 to 50. The microrotation microplar (N^*) contours have been demonstrated in the last row where the values of $|N^*_{max}|$ are 2.6630 and 1.0967 (58.8% decreasing) for Ha = 0 and Ha = 50, respectively.

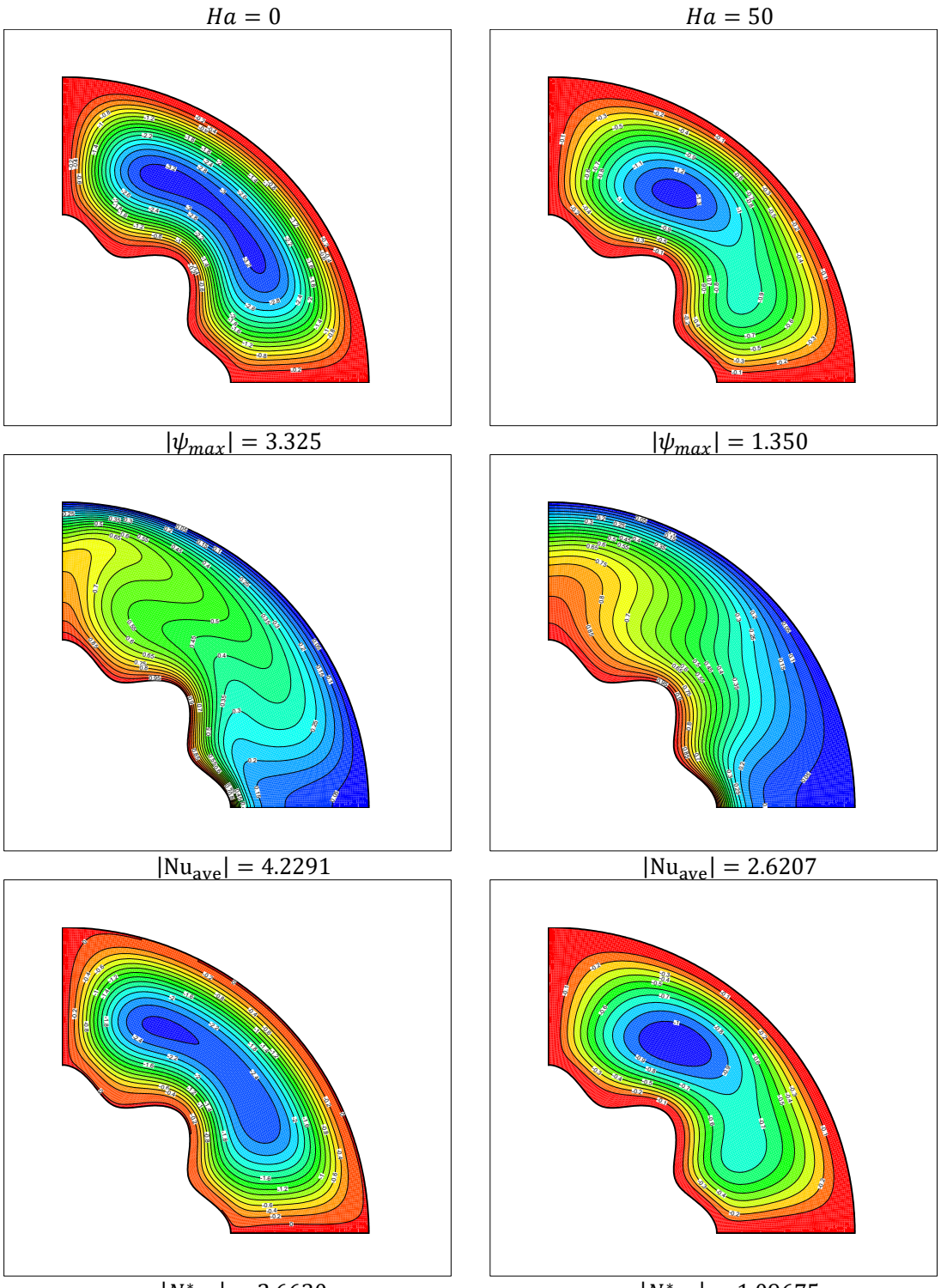

Fig. 4: Streamlines (ψ), isotherms (θ), and microrotation (N^*) contours for two values of Hartmann number

Fig. 5 presents the $\mathrm{Nu_{ave}}$ versus the angle of magnetic field (λ) for different values of Ha. The figure shows that firstly, the $\mathrm{Nu_{ave}}$ decreases, reaches to a minimum value and then increases with increasing

the magnetic field angle for each value of Ha (except Ha $= 0$). The minimum value occurs at $\lambda = 45°$ for Ha $= 25$ and at $\lambda = 30°$ for Ha $= 50$ and Ha $= 75$. Indeed, the minimum value for $\mathrm{Nu_{ave}}$ occurs when the effect of the magnetic field increases on the fluid flow and buoyancy force. The figure shows that $\mathrm{Nu_{ave}}$ decreases with ascending the Ha. For example, $\mathrm{Nu_{ave}}$ descends from 3.3036 to 1.8226 (44.83% decreasing) when Ha increases from 25 to 75 at $\lambda = 45°$.

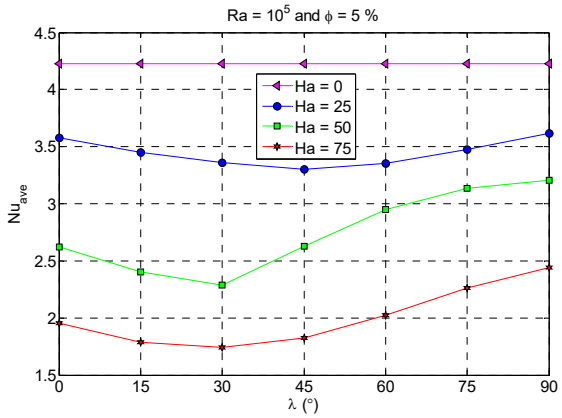

Fig. 5: Average Nusselt number versus angle of magnetic field for different Hartmann numbers for $\phi =$ 5% at $Ra = 10^5$

The impact of particle volume fraction (ϕ) on the $\mathrm{Nu_{ave}}$ is depicted in Fig. 6. In this figure $\lambda = 0^{\circ}$, $K = 2, A = 0.1, N_u = 8$ and Ra $= 10^5$ are considered. The figure demonstrates the values of the $\mathrm{Nu_{ave}}$ with respect to a reference value that is corresponding to Ha $= 0$ and $\phi = 0$. This reference values is $\mathrm{Nu_{ave,ref}} = 3.9513$. The figure shows that the $\mathrm{Nu_{ave}}$ declines when the Ha ascends while it increases when particle volume fraction increases for each Ha. The highest value of the $\mathrm{Nu_{ave}}$ is corresponding to Ha $= 0$ and $\phi = 0.04$ $\left(\mathrm{Nu_{ave}}/\mathrm{Nu_{ave,ref}} = 1.058\right)$ while its minimum value is corresponding to Ha $= 40$ and $\phi = 0$ $\left(\mathrm{Nu_{ave}}/\mathrm{Nu_{ave,ref}} = 0.706\right)$. According to Eq. (12), thermal conductivity of nanofluid increases due to increasing of ϕ and therefore, according to Eq. (23), the values of $\mathrm{Nu_{ave}}$ increase.

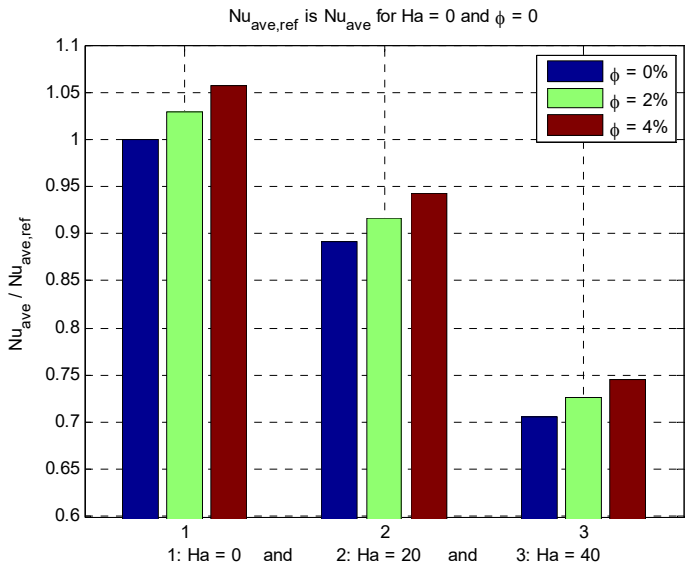

Fig. 6: The average Nusselt number for different values of particle volume fraction at various values of Hartmann number

Fig. 7 shows the effects of material parameter (K) on the isotherms, the streamlines, and microrotation contours. In this figure $\mathrm{Ha} = 0$, $\phi = 0$, $A = 0.1$, $N_u = 8$ and $\mathrm{Ra} = 10^5$ are considered. The figure shows that $|\Psi_{\max}|$ decreases from 3.893 to 3.229 (17.1% decreasing) and $\mathrm{Nu}_{\mathrm{ave}}$ descends from 4.4297 to 3.9513 (10.8% descending), while $|N^*_{\max}|$ increases from 2.2929 to 2.7462 (19.8% increasing) when K increases from 1 to 2. These results can be interpreted according to the coefficient of the first term at the RHS of Eqs. (17) and (18). When material parameter increases, it is equivalent to increasing the viscosity of the fluid, and therefore the fluid flow rate decreases.

Fig. 8 shows the effects of amplitude parameter (A) on the isotherms, the streamlines, and microrotation contours. The figure shows that when the amplitude of the undulation increases from $A = 0$ to $A = 0.2$ then $|\Psi_{\max}|$ decreases. Because the accessible volume for fluid circulation diminishes as A grows, the strength of fluid flow decreases. A decreasing trend can be observed for the values of $\mathrm{Nu}_{\mathrm{ave}}$ (52.9% decreasing) and $|N^*_{\max}|$ (7.5% decreasing) when A increases from 0 to 0.2. This is due to the fact that by increasing the amplitude parameter the fluid must travel a more meandering path from the bottom to the top of the enclosure.

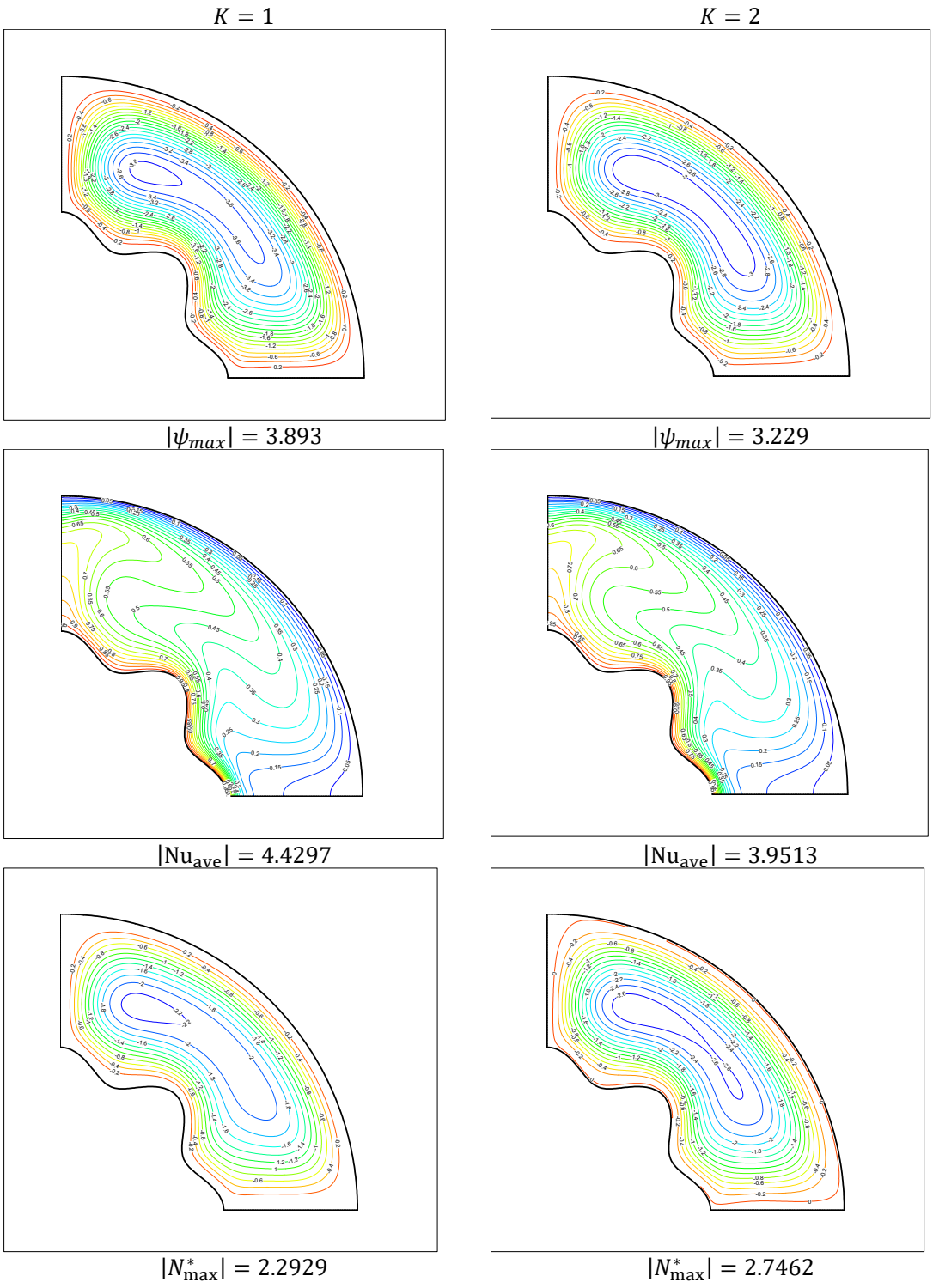

Fig. 7: Streamlines (ψ), isotherms (θ), and microrotation (N^*) contours for two values of material parameter

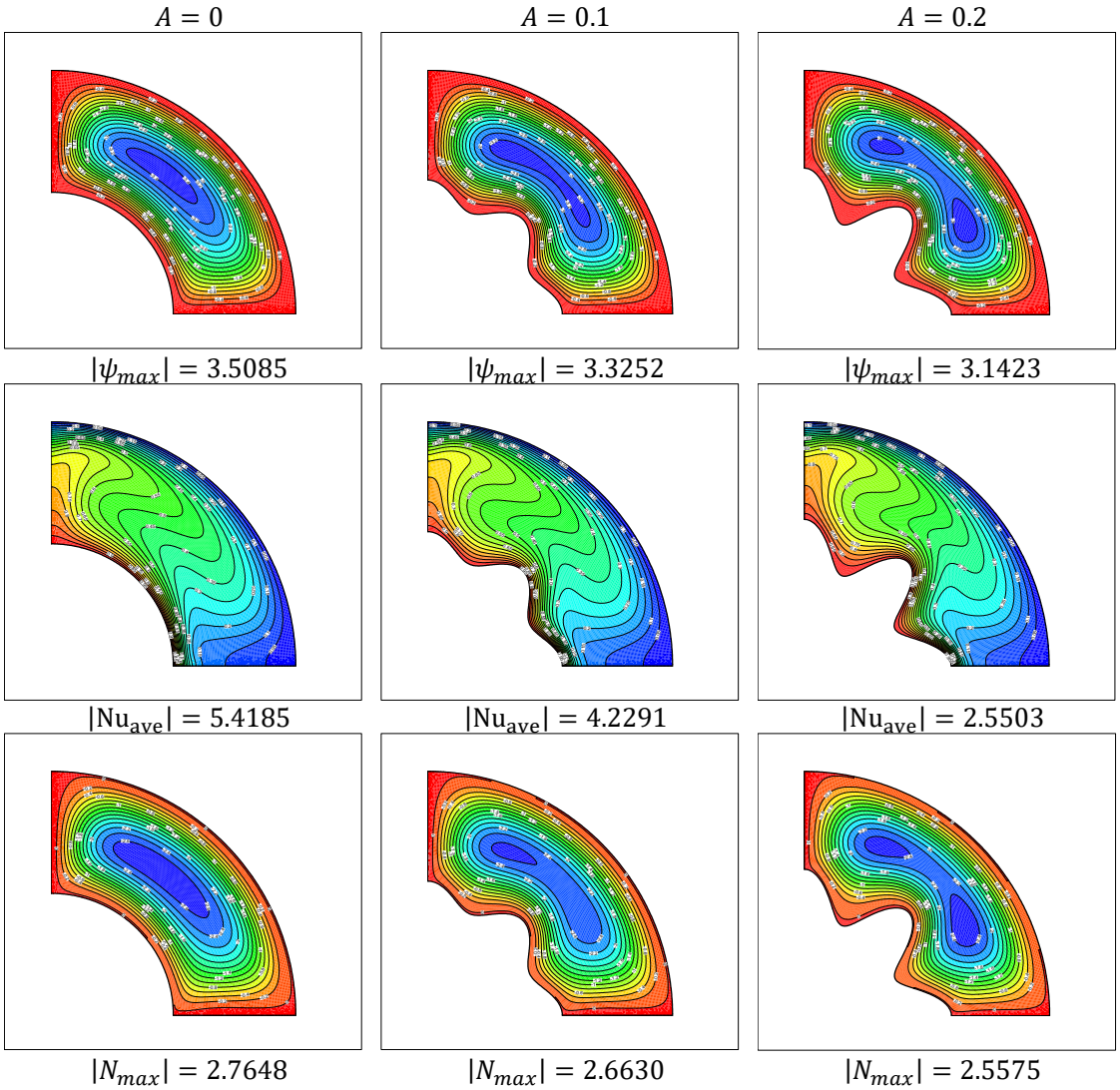

Fig. 8: Streamlines (ψ), isotherms (θ), and microrotation (N^*) contours for three values of amplitude parameter

Fig. 9(a) demonstrates the variations of $\mathrm{Nu_{ave}}$ versus the K for $A = 0$ and $A = 0.1$. The figure shows that the values of $\mathrm{Nu_{ave}}$ decrease with increasing the K for each value of A. For example, $\mathrm{Nu_{ave}}$ descends from 4.7943 to 4.1613 (13.2% descending) when K increases from 0.5 to 1.5 for $A = 0.1$. Also, the values of $\mathrm{Nu_{ave}}$ decrease with increasing the A for each value of K. This is due to the narrowing of the flow path with increasing A. For example, $\mathrm{Nu_{ave}}$ descends from 5.0437 to 3.9513 (21.7% descending) when A increases from 0 to 0.1 for $K = 2$. Fig. 9(b) demonstrates the variations of $\mathrm{Nu_{ave}}$ versus the K for $N_u = 4$, $N_u = 6$ and $N_u = 8$. The figure shows that the values of $\mathrm{Nu_{ave}}$ decrease with increasing the K for each value of N_u. For example, $\mathrm{Nu_{ave}}$ descends from 4.3861 to

3.9259 (10.5% descending) when K increases from 0.5 to 1.5 for $N_u = 6$. Also, the values of $\mathrm{Nu_{ave}}$ decrease with increasing the N_u for each value of K. This is due to the narrowing of the flow path with increasing A. For example, $\mathrm{Nu_{ave}}$ descends from 4.5881 to 3.7918 (17.4% descending) when N_u increases from 4 to 8 for $K = 1$.

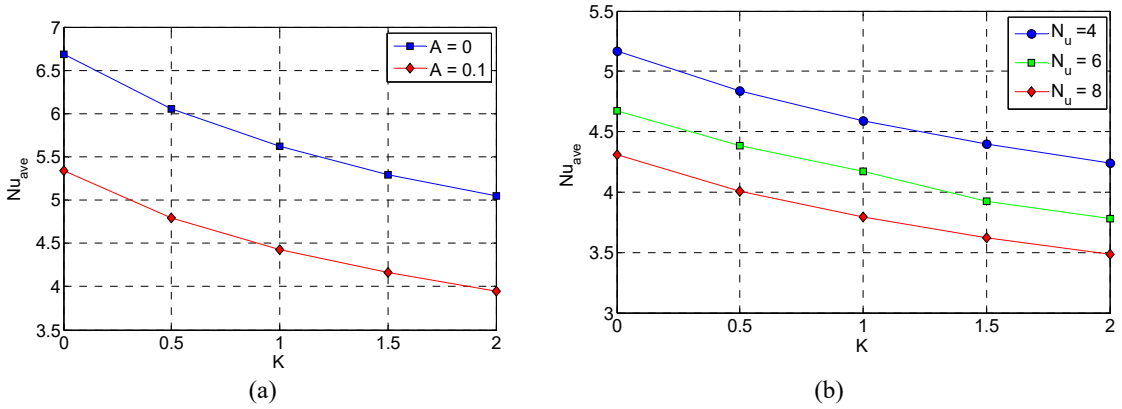

Fig. 9: The variations of $\mathrm{Nu_{ave}}$ versus the K for (a) $A = 0$ and $A = 0.1$ and (b) $N_u = 4$, $N_u = 6$, and $N_u = 8$

A novel investigation has been performed in this work. As we know, the $\mathrm{Nu_{ave}}$ increases with increasing the particle volume fraction while it decreases as the Ha increases. In other words, the decreasing of the Nusselt number due to increasing the Ha can be compensated by increasing the particle volume fraction. Fig. 10 shows the values of the $\mathrm{Nu_{ave}}$ versus the particle volume fraction. In the figure, the values of $\mathrm{Nu_{ave}}$ are 5.3394 and 3.9513 for $\phi = 0$ at $K = 0$ and $K = 2$, respectively. The figure shows that the values of Ha are 4.3, 6.0, 7.1, 8.5 and 9.4 for ϕ from 1% up to 6%, respectively at $K = 0$ where the value of $\mathrm{Nu_{ave}}$, remains constant. These values are 6.1, 9.0, 11.2, 13.1 and 14.8 for $K = 2$. For example, if the nanoparticle value is 3%, in $\mathrm{Ha} = 11.2$ for $K = 2$, the Nusselt number will not change.

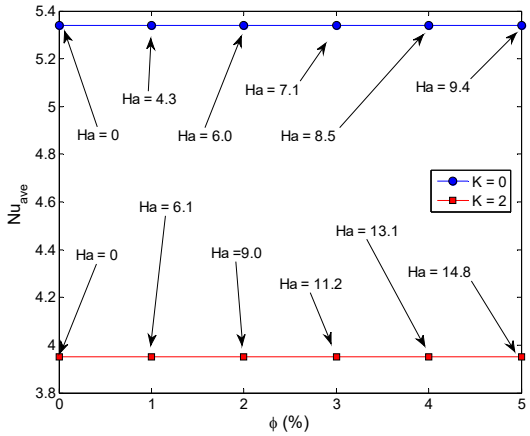

Fig. 10: The variations of $\mathrm{Nu}_{\mathrm{ave}}$ versus the ϕ for $K = 0$ and $K = 2$

Table 6 presents a comparison between the values of the $\mathrm{Nu}_{\mathrm{ave}}$ that have been obtained by FVM (ANSYS Fluent software) and CVFEM (FORTRAN Code). The last column shows the values of errors that are acceptable.

Table 6: FVM by ANSYS Fluent, CVFEM by FORTRAN Code

Case	Ra	Ha	ϕ	$\mathrm{Nu}_{\mathrm{ave}}$		
				FVM	CVFEM	Error (%)
1	10^3	10	0.04	1.2923	1.2685	+1.8
2	10^4	10	0.04	1.8058	1.7593	+2.6
3	10^5	10	0.04	4.0162	4.0405	-0.6
4	10^5	0	0.05	4.1625	4.2291	-1.6
5	10^5	50	0.05	2.5812	2.6207	-1.5

Fig. 11 shows the streamlines, isotherms microrotation, velocity field and vector of velocity contours for two values of Ha that have been obtained by Ansys Fluent. This figure is similar to Fig. 4.

Fig. 12 depicts the variations of $\mathrm{Nu}_{\mathrm{ave}}$ for different values of shape factor of nanoparticle, spherical shape ($m = 3$), cylindrical shape ($m = 4.8$) and platelet shape ($m = 5.7$) at $K = 0$ and $K = 1$. The figure discovers that the average Nusselt numbers grow when the shape factor goes up for the material parameter. For example, $\mathrm{Nu}_{\mathrm{ave}}$ increases from 4.7123 to 5.0622 (7.4%) when nanoparticles change from spherical to platelet shapes for $K = 1$. This is due to increasing the thermal conductivity of nano-fluid (See Eq. 12). In this figure $\mathrm{Ha} = 0$, $\lambda = 0^{\circ}$, $A = 0.1$, $N_u = 8$ and $\mathrm{Ra} = 10^5$ were considered.

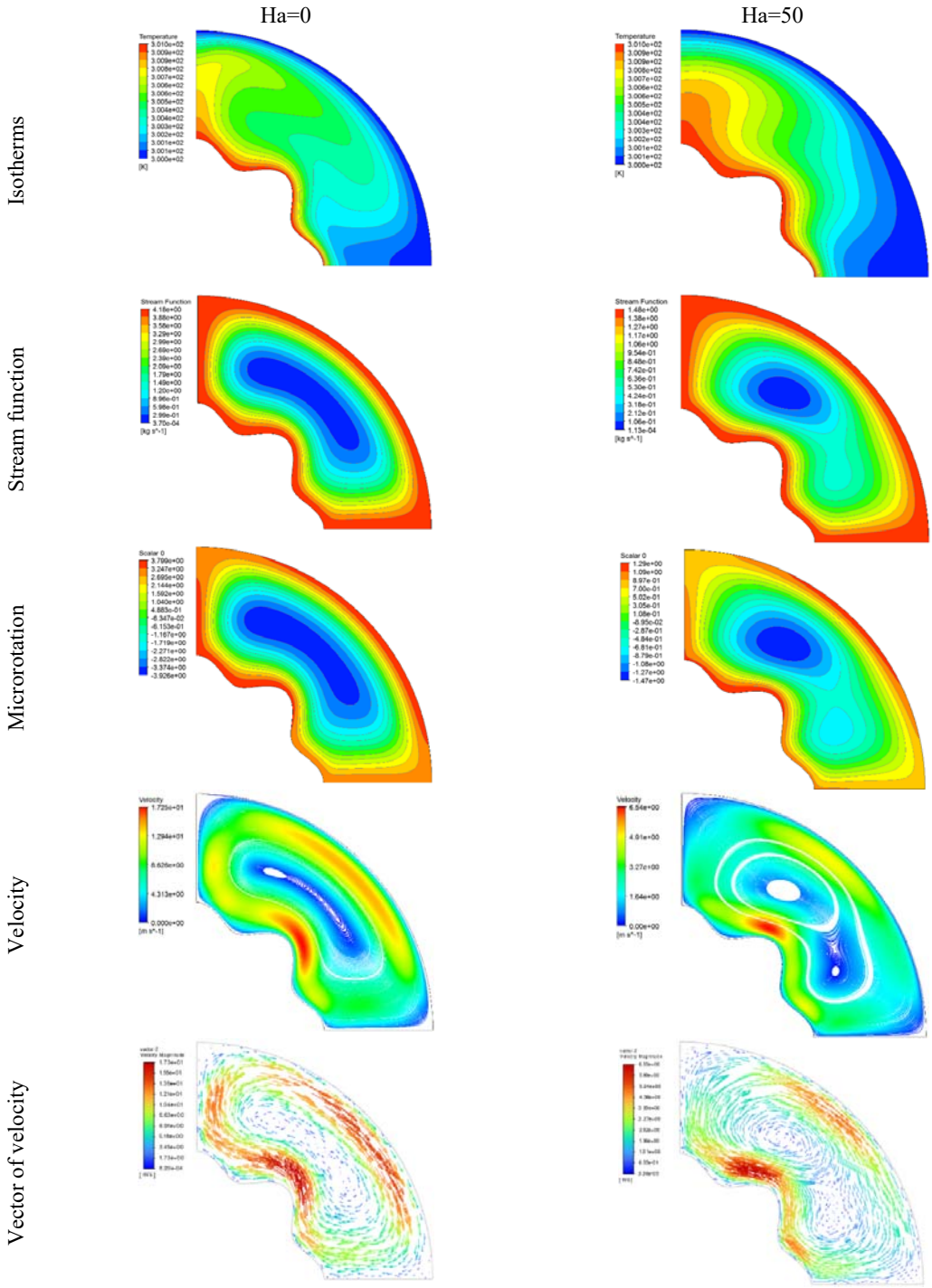

Fig. 11: Streamlines (ψ), isotherms (θ), microrotation (N^*), velocity and vector of velocity contours for two values of Hartmann number by Ansys Fluent

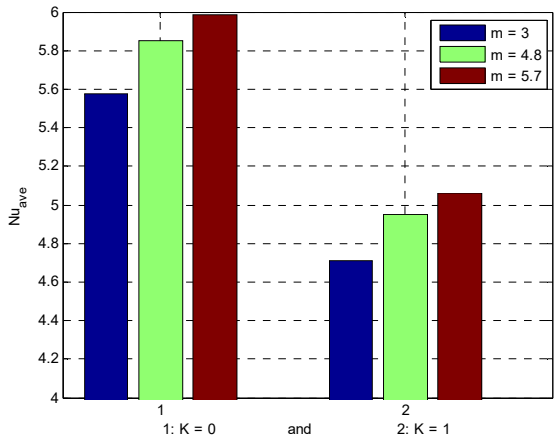

Fig. 12: The variations of $\mathrm{Nu_{ave}}$ for different values of shape factor of nanoparticle (m) at $K = 0$ and $K = 1$

Fig. 13 presents the variations of $|\psi_{max}|$ and $\mathrm{Nu_{ave}}$ versus Prandtl number for $K = 0$ and $K = 2$. The figure shows that the values of $|\psi_{max}|$ descend while the values of $\mathrm{Nu_{ave}}$ ascend with ascending Pr for the material parameter. For example, $|\psi_{max}|$ decreases from 149.86 to 0.34 (99.8% decreasing) and from 136.67 to 0.21 (99.84% decreasing) when Pr increases from 0.1 to 100 for pure fluid $(K = 0)$ and micropolar fluid $(K = 2)$, respectively. Also, $\mathrm{Nu_{ave}}$ increases from 3.9186 to 5.4920(40.2%) and from 3.4751 to 3.9709 (14.3%) when Pr increases from 0.1 to 100 for pure fluid $(K = 0)$ and micropolar fluid $(K = 2)$, respectively. In this figure ϕ is equal to zero. In this figure $\mathrm{Ha} = 0$, $\lambda = 0^{\circ}$, $A = 0.1$, $N_u = 8$ and $\mathrm{Ra} = 10^5$ were considered. This figure discovers that the velocity of fluid flow decreases while heat transfer rate increases as the Pr number increases.

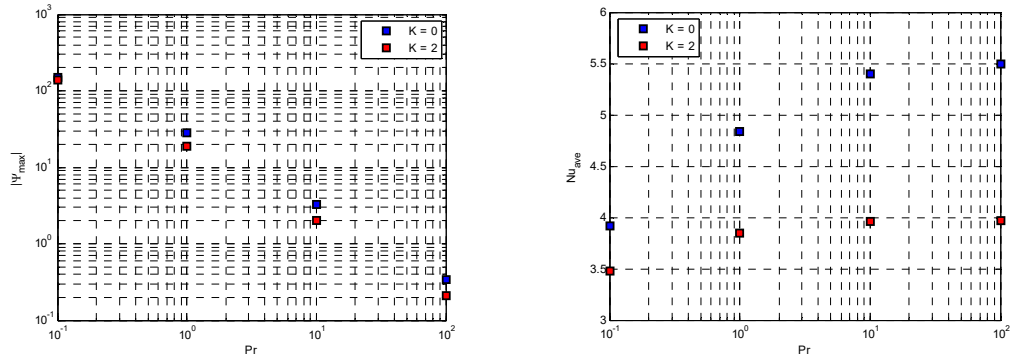

Fig. 13: The variations of $|\psi_{max}|$ and $\mathrm{Nu_{ave}}$ versus Pr number for $K = 0$ and $K = 2$

6. Conclusion

The natural-convection flow of a micropolar-nanofluid (Al_2O_3/water) in the presence of an inclined magnetic field in a semi-annulus enclosure was studied. The non-dimensional governing equations have been solved by CVFEM-Fortran code and FVM-Ansys Fluent CFD software. Here, important outcomes are recalled:

- The values of $|\Psi_{max}|$, Nu_{ave} and $|N^*_{max}|$ rises with increasing the Ra. The values of $|\Psi_{max}|$ are 0.076, 0.687 and 3.067, the values of Nu_{ave} are 1.2685, 1.7593 and 4.0405 and the values of $|N^*_{max}|$ are 0.0636, 0.5703 and 2.4873 for $Ra = 10^4, 10^5$ and 10^6, respectively. So the fluid velocity and the heat transfer rate are in direct relation with Ra (Fig. 3).
- The values of Nu_{ave} and $|N^*_{max}|$ descend 38.03% and 58.8% , respectively with ascending the Ha (Fig. 4).
- Nu_{ave} descends 44.83% when Ha increases from 25 to 75 at $\lambda = 45°$ (Fig. 5).
- $Nu_{ave}/Nu_{ave,ref} = 1.058$ is related to $Ha = 0$ and $\phi = 0.04$ and $Nu_{ave}/Nu_{ave,ref} = 0.706$ is related to $Ha = 40$ and $\phi = 0$ (Fig. 6).
- The values of $|\Psi_{max}|$ and Nu_{ave} decrease 17.1% and 10.8%, respectively while $|N_{max}|$ increases 19.8% when K increases from 1 to 2 (Fig. 7).
- The values of Nu_{ave} and $|N^*_{max}|$ descend 52.9% and 7.5% respectively when A increases from 0 to 0.2 (Fig. 8).
- Nu_{ave} descends 13.2% when K increases from 0.5 to 1.5 for $A = 0.1$ whereas it descends 17.4% when N_u increases from 4 to 8 for $K = 1$ (Fig. 9).
- The result shows that the values of Ha are 6.1, 9.0, 11.2, 13.1 and 14.8 for ϕ from 1% up to 6%, respectively at $K = 2$ (Fig. 10).
- The values of Nu_{ave} increase with ascending the value of shape factor of nanoparticle for each value of K (Fig. 12).
- The values of Nu_{ave} increase 40.2% and 14.3% when Pr increases from 0.1 to 100 for $K = 0$ and $K = 2$, respectively (Fig. 13).

Nomenclature

A	Amplitude	*Greek letter*	
B	magnetic field (T)	α	thermal diffusivity (m^2s^{-1})
B_0	magnetic field strength (T)	β	thermal expansion coefficient (K^{-1})
C_p	specific heat capacity ($J\ kg^{-1}\ K^{-1}$)	γ	spin-gradient viscosity ($kg\ m\ s^{-1}$)
g	gravitational acceleration (ms^{-2})	θ	dimensionless temperature (-)
Ha	Hartmann number (-)	κ	vortex viscosity ($kg\ m^{-1}\ s^{-1}$)
j	micro-inertia density (m^2)	λ	Inclination angle (º)
k	thermal conductivity ($Wm^{-1}K^{-1}$)	μ	dynamic viscosity ($N\ s\ m^{-2}$)
K	non-dimensional material parameter (-)	ν	kinematic viscosity (m^2s^{-1})
L	length of the cavity (m)	ζ	rotation angle (º)
M	shape factor of nanoparticle (-)	ρ	density ($kg\ m^{-3}$)
N	dimensional microrotation (s^{-1})	σ	electrical conductivity (Ω/m)
N*	dimensionless microrotation (-)	ΔT	temperature difference
N_u	number of undulations (-)	ϕ	volume fraction
Nu	Nusselt number (-)	ψ	dimensional stream function ($m^2\ s^{-1}$)
P	pressure (Nm^{-2})	Ψ	dimensionless stream function (-)
Pr	Prandtl number (-)	Ω	dimensional vorticity (s^{-1})
r	true inner wall radius (m)	Ω	dimensionless vorticity (-)
r_{in}	base circle radius (m)	*Subscripts*	
Ra	Rayleigh number (-)	ave	Average
T	temperature (K)	c	cold
u, v	dimensional x and y components of velocity ($m\ s^{-1}$)	f	fluid
x, y	dimensional coordinates (m)	h	hot
X, Y	dimensionless coordinates	nf	nanofluid
		s	solid

References

[1] S.U.S. Choi, J.A. Eastman, Enhancing thermal conductivity of fluids with nanoparticles: The Proceedings of the 1995 ASME International Mechanical Engineering Congress and Exposition, San Francisco, USA, ASME, FED 231/MD, 66 (1995) 99-105.

[2] Rashad AM, Armaghani T, Chamkha AJ, Mansour MA. Entropy generation and MHD natural convection of a nanofluid in an inclined square porous cavity: effects of a heat sink and source size and location. Chin. J. phys. 2018;56:193–211.

[3] Abu-Nada, E., Masoud, Z. and Hijazi, A., 2008. Natural convection heat transfer enhancement in horizontal concentric annuli using nanofluids. International Communications in Heat and Mass Transfer, 35(5), pp.657-665.

[4] Chamkha, A., Ismael, M., Kasaeipoor, A. and Armaghani, T., 2016. Entropy generation and natural convection of CuO-water nanofluid in C-shaped cavity under magnetic field. Entropy, 18(2), p.50.

[5] Sheikhzadeh, G.A., Arefmanesh, A., Kheirkhah, M.H. and Abdollahi, R., 2011. Natural convection of Cu–water nanofluid in a cavity with partially active side walls. European Journal of Mechanics-B/Fluids, 30(2), pp.166-176.

[6] Selimefendigil, F. and Öztop, H.F., 2015. Natural convection and entropy generation of nanofluid filled cavity having different shaped obstacles under the influence of magnetic field and internal heat generation. Journal of the Taiwan Institute of Chemical Engineers, 56, pp.42-56.

[7] Alsabery AI, Tayebi T, Chamkha AJ, Hashim I. Natural convection of Al2O3-water nanofluid in a non-Darcian wavy porous cavity under the local thermal non-equilibrium condition. Sci. Rep. 2020;10:18048.

[8] Aly, A.M., Mohamed, E.M. and Alsedais, N., 2021. The magnetic field on a nanofluid flow within a finned cavity containing solid particles. Case Studies in Thermal Engineering, 25, p.100945.

[9] Gholamalipour, P., Siavashi, M. and Doranehgard, M.H., 2019. Eccentricity effects of heat source inside a porous annulus on the natural convection heat transfer and entropy generation of Cu-water nanofluid. International Communications in Heat and Mass Transfer, 109, p.104367.

[10] Tayebi, T. and Chamkha, A.J., 2020. Entropy generation analysis due to MHD natural convection flow in a cavity occupied with hybrid nanofluid and equipped with a conducting hollow cylinder. Journal of Thermal Analysis and Calorimetry, 139(3), pp.2165-2179.

[11] Gorla, R.S.R., Siddiqa, S., Mansour, M.A., Rashad, A.M. and Salah, T., 2017. Heat source/sink effects on a hybrid nanofluid-filled porous cavity. Journal of Thermophysics and Heat Transfer, 31(4), pp.847-857.

[12] Seyyedi, S.M., Hashemi-Tilehnoee, M. and Sharifpur, M., 2021. Effect of Inclined Magnetic Field on the Entropy Generation in an Annulus Filled with NEPCM Suspension. Mathematical Problems in Engineering, 2021, Article ID 8103300.

[13] Seyyed Masoud Seyyedi, M. Hashemi-Tilehnoee, M. Sharifpur, Impact of Fusion Temperature on Hydrothermal Features of Flow within an Annulus Loaded with Nanoencapsulated Phase Change Materials (NEPCMs) during Natural Convection Process, Mathematical Problems in Engineering, 2021, Article ID 4276894.

[14] Abdel-Nour, Z., Aissa, A., Mebarek-Oudina, F., Rashad, A.M., Ali, H.M., Sahnoun, M. and El Ganaoui, M., 2020. Magnetohydrodynamic natural convection of hybrid nanofluid in a porous enclosure: numerical analysis of the entropy generation. Journal of Thermal Analysis and Calorimetry, 141(5), pp.1981-1992.

[15] Seyyed Masoud Seyyed, A.S. Dogonchi, D.D. Ganji, M. Hashemi-Tilehnoee, Entropy generation in a nanofluid-filled semi-annulus cavity by considering the shape of nanoparticles, J. Therm. Anal. Calorim. (2019) 1–15.

[16] Hashemi-Tilehnoee, M., Dogonchi, A.S., Seyyedi, S.M. and Sharifpur, M., 2020. Magneto-fluid dynamic and second law analysis in a hot porous cavity filled by nanofluid and nano-encapsulated phase change material suspension with different layout of cooling channels. Journal of Energy Storage, 31, p.101720.

[17] Seyyed Masoud Seyyedi, A.S. Dogonchi, M. Hashemi-Tilehnoee, Zeeshan Asghar, M. Waqas, D.D. Ganji, A computational framework for natural convective hydromagnetic flow via inclined cavity: an analysis subjected to entropy generation, J. Mol. Liq. 287 (2019) 110863.

[18] Seyyed Masoud Seyyedi, A.S. Dogonchi, R. Nuraei, D.D. Ganji, M. HashemiTilehnoee, Numerical analysis of entropy generation of a nanofluid in a semi-annulus porous enclosure with different nanoparticle shapes in the presence of a magnetic field, Eur. Phys. J. Plus 134 (2019) 268.
[19] Eringen, A.C., 1964. Simple microfluids. International Journal of Engineering Science, 2(2), pp.205-217.
[20] Eringen, A.C., 1972. Theory of thermomicrofluids. Journal of Mathematical analysis and Applications, 38(2), pp.480-496.
[21] Aydin, O. and Pop, I., 2005. Natural convection from a discrete heater in enclosures filled with a micropolar fluid. International journal of engineering science, 43(19-20), pp.1409-1418.
[22] Aydin, O. and Pop, I., Natural convection in a differentially heated enclosure filled with a micropolar fluid, International Journal of Thermal Sciences 46 (2007) 963–969
[23] Saleem, M., Asghar, S. and Hossain, M.A., 2011. Natural convection flow of micropolar fluid in a rectangular cavity heated from below with cold sidewalls. Mathematical and Computer Modelling, 54(1-2), pp.508-518.
[24] Mehryan, S.A.M., Izadi, M. and Sheremet, M.A., 2018. Analysis of conjugate natural convection within a porous square enclosure occupied with micropolar nanofluid using local thermal non-equilibrium model. Journal of Molecular Liquids, 250, pp.353-368.
[25] Ahmed, S.E. and Rashad, A.M., 2016. Natural convection of micropolar nanofluids in a rectangular enclosure saturated with anisotropic porous media. Journal of Porous Media, 19(8).
[26] Yan, S.R., Izadi, M., Sheremet, M.A., Pop, I., Oztop, H.F. and Afrand, M., 2020. Inclined Lorentz force impact on convective-radiative heat exchange of micropolar nanofluid inside a porous enclosure with tilted elliptical heater. International Communications in Heat and Mass Transfer, 117, p.104762.
[27] Karagiannakis, N.P., Bourantas, G.C., Skouras, E.D., Loukopoulos, V.C., Miller, K. and Burganos, V.N., 2020. Modeling the natural convection flow in a square porous enclosure filled with a micropolar nanofluid under magnetohydrodynamic conditions. Applied Sciences, 10(5), p.1633.
[28] Izadi, M., Sheremet, M.A., Mehryan, S.A.M., Pop, I., Öztop, H.F. and Abu-Hamdeh, N., 2020. MHD thermogravitational convection and thermal radiation of a micropolar nanoliquid in a porous chamber. International Communications in Heat and Mass Transfer, 110, p.104409.
[29] Kai-Long Hsiao, To Promote Radiation Electrical MHD Activation Energy Thermal Extrusion Manufacturing System Efficiency by Using Carreau-Nanofluid with Parameters Control Method, Energy, 130 (2017) 486-499.
[30] Kai-Long Hsiao, Combined Electrical MHD Heat Transfer Thermal Extrusion System Using Maxwell Fluid with Radiative and Viscous Dissipation Effects, Applied Thermal Engineering, 112(2017)1281-1288.
[31] Kai-Long Hsiao, Micropolar Nanofluid Flow with MHD and Viscous Dissipation Effects Towards a Stretching Sheet with Multimedia Feature, International Journal of Heat and Mass Transfer, 112 (2017) 983-990.

[32] Kai-Long Hsiao, Stagnation Electrical MHD Nanofluid Mixed Convection with Slip Boundary on a Stretching Sheet, Applied Thermal Engineering, 98 (2016) 850-861.
[33] Seyyed Masoud Seyyedi A.S. Dogonchi, M. Hashemi-Tilehnoee, M. Waqas, D.D. Ganji, Entropy generation and economic analyses in a nanofluid filled L shaped enclosure subjected to an oriented magnetic field, Appl. Therm. Eng. 168 (2020) 114789.
[34] G. de Vahl Davis, Natural convection in a square cavity: A bench mark solution, Int. J. Numer. Method Fluids 3 (1983) 249–264.
[35] H.J. Saabas, B.R. Baliga, Co-located equal-order control-volume finite-element method for multidimensional, incompressible. Fluid flow-part I: formulation, Numer. Heat Transf. 26 (4) (1994) 381–407.
[36] Matej Zadravec, Matjaz Hribersek, Leopold Skerget, Natural convection of micropolar fluid in an enclosure with boundary element method, Engineering Analysis with Boundary Elements 33 (2009) 485–492
[37] M. Pirmohammadi, M. Ghassemi, G.A. Sheikhzadeh, The effect of a magnetic field on buoyancy-driven convection in differentially heated square cavity, 2008 14th Symposium on Electromagnetic Launch Technology, IEEE, 2008, pp. 1–6.
[38] M. Hashemi-Tilehnoee, N. Sahebi, A.S. Dogonchi, S.M. Seyyedi, S Tashakor, Simulation of the dynamic behavior of a rectangular single-phase natural circulation vertical loop with asymmetric heater, Int J Heat Mass Transf 139 (2019) 974–981.
[39] M. Hashemi-Tilehnoee, S. Tashakor, S.M. Seyyedi, N Sahebi, Forced refood modeling in a 2 × 2 rod bundle with a 90% partially blocked region, Ann. Nucl. Energy 131 (2019) 425–432.
[40] M. Hashemi-Tilehnoee, S. Tashakor, A.S. Dogonchi, S.M. Seyyedi, M. Khaleghi, Entropy generation in concentric annuli of 400kV gas-insulated transmission line, Therm. Sci. Eng. Progress 19 (2020) 100614 Inpress.
[41] M. Karami, S. Tashakor, A. Afsari, M Hashemi-Tilehnoee, Effect of the baffle on the performance of a micro pin fin heat sink, Therm. Sci. Eng. Progr. 14 (2019) 100417.
[42] Hashemi-Tilehnoee, M., del Barrio, E.P. and Seyyedi, S.M., 2022. Magneto-turbulent natural convection and entropy generation analyses in liquid sodium-filled cavity partially heated and cooled from sidewalls with circular blocks. International Communications in Heat and Mass Transfer, 134, p.106053.
[43] Hashemi-Tilehnoee, M. and del Barrio, E.P., 2022. Magneto laminar mixed convection and entropy generation analyses of an impinging slot jet of Al2O3-water and Novec-649. Thermal Science and Engineering Progress, 36, p.101524.

Appendix

The control volume finite element method (CVFEM) combines interesting characteristics from both the FVM (finite volume method) and FEM (finite element method). The CVFEM was firstly introduced by Saabas and Baliga [35]. A CVFEM algorithm can be found in Ref. [33]. Fig.A.1 represents a flowchart for CVFEM.

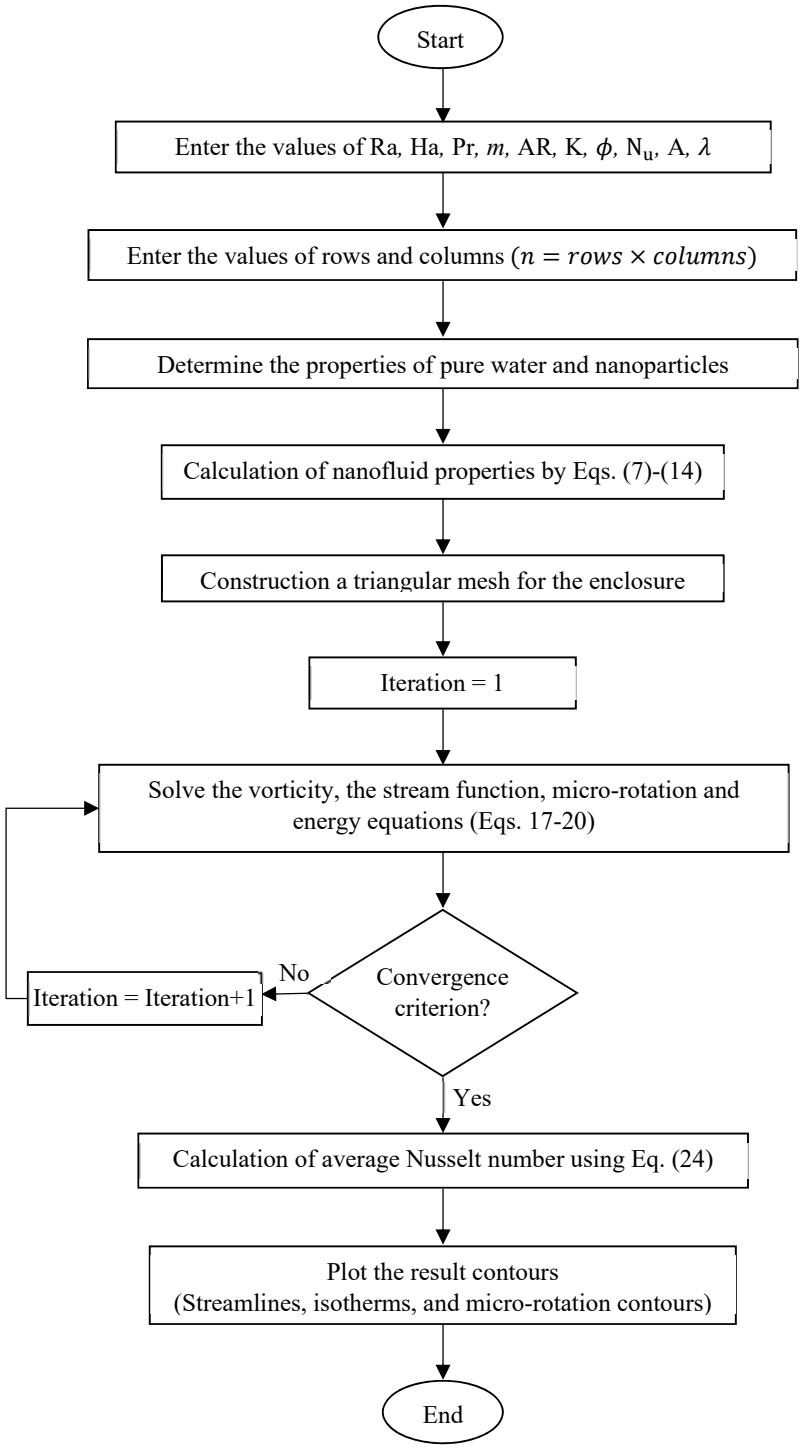

Fig. A.1: The flowchart for CVFEM

```
cols=81, rows = 241

rout = 2, rin=1

A = 0.1, Nu = 8

do k=1 , rows
do j=1 , cols
    theta = 2 * atan(1.) * (k - 1) / (rows - 1);
    radius = rin + A * cos(Nu * theta) + (rout - rin - A * cos(Nu * theta)) * (j - 1) / (cols - 1);
i=j+(k-1)*cols
y(i)=radius * sin(theta)
x(i)=radius * cos(theta)
enddo
enddo
```

Fig. A.2: A pseudo-code for transferring from physical domain to calculation domain